Inverse problem approach for particle digital holography: accurate location based on local optimisation

Ferréol Soulez, Loïc Denis, Corinne Fournier, Éric Thiébaut, Charles Goepfert

Inverse problem approach for particle digital holography: accurate location based on local optimisation

Ferréol Soulez*
Université de Lyon, Lyon, F-69000, France ;
Université Lyon 1, Villeurbanne, F-69622, France ;
Centre de Recherche Astronomique de Lyon,
Observatoire de Lyon, 9 avenue Charles André,
Saint-Genis Laval cedex, F-69561, France ; CNRS,
UMR 5574 ; Ecole Normale Supérieure de Lyon, Lyon, France
and
Laboratoire Hubert Curien (ex-LTSI) ; CNRS, UMR5516 ; Université Jean Monnet
18 rue Pr Benoît Lauras, F-42000 Saint-Etienne, France

Loïc Denis and Corinne Fournier
Laboratoire Hubert Curien (ex-LTSI) ; CNRS, UMR5516 ; Université Jean Monnet
18 rue Pr Benoît Lauras, F-42000 Saint-Etienne, France

Éric Thiébaut
Université de Lyon, Lyon, F-69000, France ;
Université Lyon 1, Villeurbanne, F-69622, France ;
Centre de Recherche Astronomique de Lyon,
Observatoire de Lyon, 9 avenue Charles André,
Saint-Genis Laval cedex, F-69561, France ; CNRS,
UMR 5574 ; Ecole Normale Supérieure de Lyon, Lyon, France

Charles Goepfert
Laboratoire de Mécanique des Fluides et d'Acoustique,
CNRS UMR 5509 ; Ecole Centrale de Lyon ; Université Lyon 1 ; INSA Lyon,
36 avenue Guy-de-Collongue F-69134 ECULLY cedex,France

This paper proposes a new micro-particles localization scheme in digital holography. Most conventionnal digital holography methods, are based on Fresnel transform and have several issues such as twin-image, border effects... To avoid these difficulties, we propose an inverse problem approach, which yields the optimal particles set which best models the observed hologram image. We resolve this global optimization problem by conventional particle detection followed by a local refinement for each particle. Results on both simulated and real digital holograms show strong improvements in the localization of the particles, particularly along the depth dimension. In our simulations, the position precision is about or better than 1 µm rms. Our results also show that the localization precision does not deteriorate for particles near the edges of the field of view.

OCIS codes: 090.1760, 100.3190, 100.5010, 100.6640, 100.2000

1. Introduction

The potential of in-line holography to analyse flow by means of particles, has been noted since its very beginnings[1]. The development of optical holography applications in fluid mechanics[2,3] established the capability of holography to give access to both particle size and tridimensional position. In-line holography is a technique which allows a description of a three-dimensional (3D) image of micro-objects to be stored on a bi-dimensional (2D) detector. The digital version of holography suppresses the wet chemical processing step by recording the hologram directly on a numerical sensor. Numerical processing makes it possible to acquire volume objects within a short time. This is particularly interesting for high speed phenomena analysis as in fluid mechanics.

Over the past decade, many contributions have been

*Electronic address: ferreol.soulez@obs.univ-lyon1.fr

made in the field of digital hologram processing in order to improve the measurement accuracy of the localization of micro-objects. The two main steps of the numerical processing are: a numerical reconstruction step to obtain a synthesized 3-D image with focused particles, and a segmentation step to extract locations and sizes of the particles from this 3-D distribution.

The reconstruction step is classically done by numerical simulation of the hologram diffraction, consisting in a Fresnel transform of the hologram at different distances z from the hologram. This approach has been well described by Kreis[4], and expressed as a discrete wavelet transform by Liebling[5]. Improved reconstruction schemes by means of filtering have also been introduced to suppress artefacts, *e.g.* double peak phenomenon[6], to improve the depth precision[7] or to reduce the twin-image noise[8].

The segmentation step consists of finding the location of each particle in the reconstructed 3-D distribution. The segmentation can be obtained by analyzing the gray levels in the volume (thresholding)[9,10]. Some authors also build their analysis on the reconstructed complex-amplitude[11].

Let us notice that the reconstruction step is time consuming and generates a huge volume of data to process. Consequently, several processing schemes based on a direct analysis of the hologram have been proposed[12,13].

To summarize, the most important issues in digital holography are:

- Limited depth resolution: The depth resolution is given by[14] $\delta z \geq \lambda/\Omega^2$ where λ is the wavelength and Ω is the numerical aperture of the imaging setup which may be limited by the size of the sensor. Usually Ω is less than 0.1 and hence $\delta z \geq 100\,\lambda$. The lateral resolution is given by $\delta x = \lambda/\Omega$ and is therefore better than the depth resolution, *e.g.* for $\Omega \leq 0.1$, $\delta x \geq 10\,\lambda$.

- Field of view limitations: With the classical in-line holography setup, *i.e.* with a collimated reference wave, the field of view is limited transversally by the detector size, typically $1\,\text{cm} \times 1\,\text{cm}$. The accuracy of the measurements for particles whose transversal position lie near the edges of the detector is much worse than for particles near the center of the detector. In practice, this limits the transversal field of view to the central part of the detector.

- Processing time: Existing algorithms are too slow (about 15 minutes to process a single hologram) for real-time processing of hologram images. Unless the processing time is significantly reduced, this slowness can also severly restrain the post-processing of data from high frame rate cameras required for tracking particles.

In this paper, we propose a new method allowing a fine location of the particles and improving the transversal field of view. Our processing is based on an inverse problem approach. In the field of digital holography, Sotthivirat and Fessler[15] have also followed an inverse problem scheme but that was to estimate a 3D surface not for particles detection.

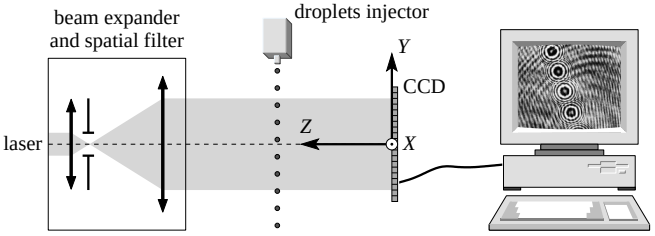

Fig. 1. In-line holography setup.

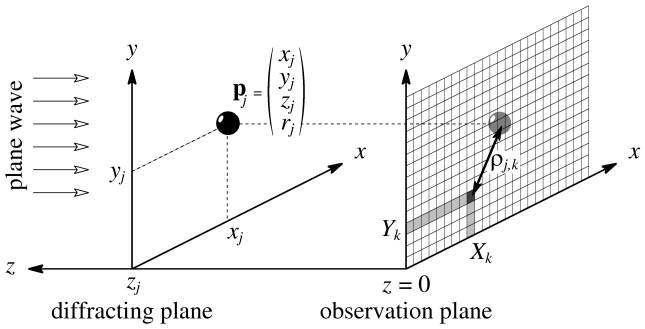

Fig. 2. Notations used in the hologram model. The parameters $\mathbf{p}_j = \{x_j, y_j, z_j, r_j\}$ are the position and radius of the j-th particle, (X_k, Y_k) is the location of the k-th pixel and $\rho_{j,k}$ is the distance between the projection of the j-th particle on the detector and the k-th pixel.

In this approach we search for the set of particle sizes and positions yielding a hologram model which best fits the real hologram image. Stated like this, the problem requires global optimization over the space of particle parameters. We effectively solve this global optimization problem by an iterative algorithm which alternates coarse location of the particles and local optimization. Since the signature of a given particle is severly disturbed by the patterns due to the other particles, we achieve an improved sensitivity to the detection and location of faint particle signatures, by repeating our processing over the residual images. Our new algorithm gives an improved precision of the particle locations, in particular along the depth dimension, and increases the size of the effective transversal field of view.

The paper is organized as follows. First, we recall the model of the hologram formation and introduce the mathematical notation used throughout the paper. Then we detail the principle of the proposed algorithm. Finally, we apply our method to the reconstruction of holograms using both simulated and real world data.

2. Model of the hologram image

In-line holography is one of the most classical techniques in holography. In this simple setup (see Fig. 1), every optical apparatus (laser, optics and camera) is aligned, studied particles are illuminated with a collimated laser beam, and both the object wave (scattered light) and the reference wave (laser) are interfering and recorded on a digital camera. In this section, we derive the model of the observed holograms under Fresnel's diffraction approximation. This model will be the basis of our fine particle positionning approach in section 3 B. The resulting hologram expression is a sum of terms depending on the position and size of each diffracting particle. Figure 2 summarizes the notation and coordinate system used in our model.

We consider an incident beam of complex amplitude $\underline{A_0}$ which is diffracted by opaque spherical particles of radii r_j and coordinates (x_j, y_j, z_j). In the remainder, underligned symbols denote complex quantities. We work under Fresnel approximation, *i.e.* the distance z between a diffracting particle and the observation plane is such that[16] $z^3 \gg 4\pi\, r_j^4/\lambda$ achieved for $z \gtrsim 1\,\text{mm}$ when $r_j \approx 50\,\mu\text{m}$ is the largest particle's axis and $\lambda = 532\,\text{nm}$ is the laser wavelength. In this case, the complex amplitude in the observation plane, *i.e.* at depth $z = 0$, diffracted by a single particle j is[16]:

$$\underline{A_j}(x,y) = \underline{A_0}\left[1 - \eta_j \left(\vartheta_j * \underline{h_{z_j}}\right)(x - x_j, y - y_j)\right] \quad (1)$$

where $*$ denotes 2-D convolution along x and y dimensions, ϑ_j is the binary apperture of the opaque particle defined by

$$\vartheta_j(x,y) = \begin{cases} 1 & \text{if} \quad \sqrt{x^2+y^2} \leq r_j \\ 0 & \text{if} \quad x > r_j \end{cases} \quad (2)$$

and $\underline{h_{z_j}}$ is the Fresnel function:

$$\underline{h_{z_j}}(x,y) = \frac{1}{\mathrm{i}\,\lambda\, z_j} \exp\left(\mathrm{i}\,\frac{\pi}{\lambda\, z_j}(x^2+y^2)\right) \quad (3)$$

where $\mathrm{i} = \sqrt{-1}$. In Eq. 1, we introduce the real factor η_j to account for possible variation of incident energy seen by a particle due to non-uniform laser illumination.

Neglecting wave front distortion due to successive particles, the complex amplitude in the observation plane diffracted by n particles of coordinates (x_j, y_j, z_j) becomes:

$$\underline{A}(x,y) = \underline{A_0}\left[1 - \sum_{j=1}^{n} \eta_j \left(\vartheta_j * \underline{h_{z_j}}\right)(x - x_j, y - y_j)\right] \quad (4)$$

For spherical particles of radius r_j small enough to have $z_j \gg 4\, r_j^2/\lambda$, the convolution product $\vartheta_j * \underline{h_{z_j}}$ can be approximated by[17]:

$$(\vartheta_j * \underline{h_{z_j}})(x,y) \simeq \frac{r_j\, \lambda\, z_j}{2\sqrt{x^2+y^2}}\, \mathrm{J}_1\left(\frac{2\,\pi\, r_j \sqrt{x^2+y^2}}{\lambda\, z_j}\right) \underline{h_{z_j}}(x,y) \quad (5)$$

where J_1 is the first order Bessel function. Since, $z_j \approx 250\,\text{mm}$ in our setup, the approximation is valid for particles such that $r_j \lesssim 60\,\mu\text{m}$. The complex amplitude $\underline{f_j}(x,y)$ of the wave diffracted by a single particle at coordinates (x_j, y_j, z_j) and observed at position $(x, y, z=0)$ therefore reads:

$$\underline{f_j}(x,y) = \frac{r_j}{2\,\mathrm{i}\,\rho_j(x,y)}\, \mathrm{J}_1\left(\frac{2\,\pi\, r_j\, \rho_j(x,y)}{\lambda\, z_j}\right) \exp\left(\mathrm{i}\,\frac{\pi\, \rho_j^2(x,y)}{\lambda\, z_j}\right) \quad (6)$$

where $\rho_j(x,y) = \sqrt{(x-x_j)^2 + (y-y_j)^2}$ is the distance between the point $(x, y, z=0)$ of the observation plane and the projection $(x_j, y_j, z=0)$ of the position of the j-th particle on the detector at $z = 0$. Thus, for n particles of parameters $\{x_j, y_j, z_j, r_j; j = 1, \ldots, n\}$ the complex amplitude at the position (x,y) of the observation plane becomes:

$$\underline{A}(x,y) = \underline{A_0}\left[1 - \sum_{j=1}^{n} \eta_j\, \underline{f_j}(x,y)\right]. \quad (7)$$

The intensity measured by the detector at position (x,y) is given by:

$$\begin{aligned} I(x,y) &= \gamma\, |\underline{A}(x,y)|^2 + I_{\text{bg}} \\ &= \gamma\, \left|\underline{A_0}\right|^2 + I_{\text{bg}} - 2\,\gamma\, \left|\underline{A_0}\right|^2 \sum_{j=1}^{n} \eta_j\, \mathrm{Re}\big(\underline{f_j}(x,y)\big) \\ &\quad + \gamma\, \left|\underline{A_0}\right|^2 \sum_{i=1}^{n}\sum_{j=1}^{n} \eta_i\, \underline{f_i}(x,y)\, \eta_j\, \underline{f_j^*}(x,y) \end{aligned} \quad (8)$$

where γ accounts for the quantum efficiency and the conversion factor of the detector whereas I_{bg} accounts for the detector background level and for other spurious emission sources if any.

In Eq. 8, η_j and f_j are adimensional. Moreover, $|\eta_j| \leq 1$ and from Eq. 6 under condition described above ($z_j \approx 250\,\text{mm}$ and $r_j \lesssim 55\,\mu\text{m}$), we found:

$$2\sum_{j=1}^{n} \eta_j\, \mathrm{Re}\big(\underline{f_j}(x,y)\big) >> \sum_{i=1}^{n}\sum_{j=1}^{n} \eta_i\, \underline{f_i}(x,y)\, \eta_j\, \underline{f_j^*}(x,y)$$

for most (x,y). So the second order terms (interferences) can be neglected and the intensity simplifies to:

$$I(x,y) = I_0 - \sum_{j=1}^{n} \alpha_j\, \mathrm{Re}\big(\underline{f_j}(x,y)\big) \quad (9)$$

where $\alpha_j = 2\,\gamma\, \left|\underline{A_0}\right|^2 \eta_j$ and $I_0 = \gamma\, \left|\underline{A_0}\right|^2 + I_{\text{bg}}$ is the image level given by the detector under the laser illumination but without diffracting particles. In the following, we will make use of the hologram model given by Eq. 6 and Eq. 9 and assume the same approximations which lead to these equations.

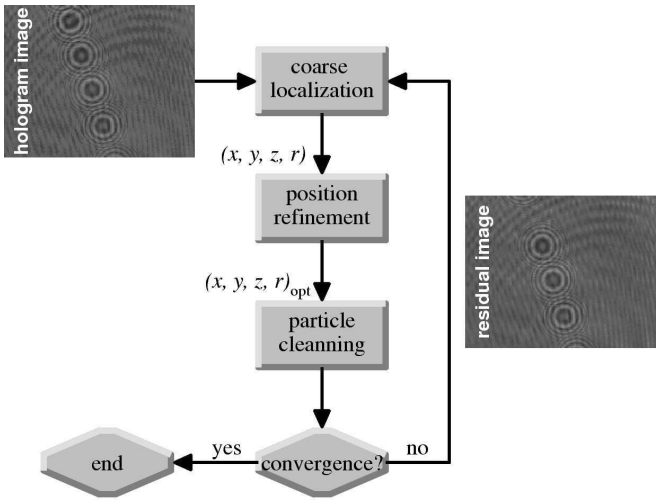

Fig. 3. Synopsis of the method.

3. Iterative algorithm

Holograms are classically processed by detecting local maxima in the probed volume reconstructed by an approximate inverse transform (as explained in section 3 A). We suggest here an improved processing which performs in three steps per particle. First, the particle with maximum contribution is located (using classical coarse localization). Then, the position of this particle is refined by searching for the set of parameters $\{x_j, y_j, z_j, r_j\}$ which minimizes the difference between the observed hologram and the hologram model. Finally, the contribution of the particle to the hologram is substracted and the same steps can be repeated to detect and localize a new particle in the residual image. These iterations are performed until no significant particle can be detected in the residuals.

A. *Particle detection*

This first step consists of finding the approximate location and size of a particle from a (residual) hologram image. This step can be carried out by existing algorithms. For instance, under Fresnel approximation, the hologram can be numerically convolved with Fresnel kernel $\underline{h_z}$ to approximately reverse the diffraction phenomenon at a given distance[4]. Indeed, by changing the distance parameter z, the reconstructed volume can be scanned in order to locate particles by digital focusing. Thus, when the reconstruction distance matches the actual distance of the particle, a minimum of amplitude is reached. This so-called maximum of focus can be derived from the reconstructed volume after thresholding by computing the centroid of the segmented 3-D particle-image. Such a detection procedure is classically performed for particle-hologram processing, but it has a limited accuracy and is prone to artifacts. The next steps of our algorithm are intended to refine the particle location.

B. *Fine particle positionning*

After the coarse detection of a new particle, the parameters $\{\alpha_n, x_n, y_n, z_n, r_n\}$ of the newly detected particle can be refined using a local optimization technique. To that end, we perform a non-linear fit of the hologram model to the hologram image by minimizing the weighted least-squares penalty:

$$\mathcal{P}_n = \sum_{k=1}^{N_{\text{pixel}}} W_k \, [M_{n,k} - D_k]^2 \tag{10}$$

where D_k is the k-th pixel value of the observed hologram and $W_k = 1/\operatorname{Var}(D_k)$ is its statistical weight. The model $M_{n,k}$ for n particles is directly given by Eq. 9:

$$M_{n,k} = I_0 - \sum_{j=1}^{n} \alpha_j \, \operatorname{Re}\big(\underline{f_j}(X_k, Y_k)\big) \,, \tag{11}$$

where (X_k, Y_k) are the coordinates of the k-th pixel.

1. Reparametrization

In order to simplify the equations and reduce the condition number of the optimization problem (which should improve the convergence rate of the fit), we introduce the following dimensionless variables:

$$x' = x/\omega \,, \quad y' = y/\omega \,, \quad z' = \lambda\, z/\omega^2 \,, \quad \text{and} \quad r' = r/\omega$$

where ω is the pixel width and we define:

$$\begin{aligned} g_j(x', y') &= \operatorname{Re}\big(\underline{f_j}(\omega\, x', \omega\, y')\big) \\ &= \frac{r'_j}{2\,\rho'_j} \, \mathrm{J}_1\left(\frac{2\,\pi\, r'_j\, \rho'_j}{z'_j}\right) \sin\left(\frac{\pi\, {\rho'_j}^2}{z'_j}\right) \end{aligned} \tag{12}$$

where $\rho'_j = \sqrt{(x'_j - x')^2 + (y'_j - y')^2}$. Our model now reads:

$$M_{n,k} = I_0 - \sum_{j=1}^{n} \alpha_j \, g_j(X'_k, Y'_k) \,, \tag{13}$$

where $(X'_k, Y'_k) = (X_k/\omega, Y_k/\omega)$ are the coordinates of the k-th image pixel in pixel units.

2. Partial local optimization

In order to speed up the non-linear fit, we make use of two tricks in the local optimization.

First, we only consider optimizing on the constant level I_0 and on the parameters of the last particle. In other words, we minimize $\mathcal{P}_n$ with respect to the parameters $\{I_0, \alpha_n, x'_n, y'_n, z'_n, r'_n\}$ and consider the other particle parameters as fixed. This is the same as fitting the parameters $\{I_0, \alpha_n, x'_n, y'_n, z'_n, r'_n\}$ on the residual image $R_{n-1,k}$ after having subtracted the contribution of the previous $n-1$ particles:

$$R_{n-1,k} = D_k + \sum_{j=1}^{n-1} \alpha_j \, g_j(X'_k, Y'_k) \,, \tag{14}$$

where, of course, $R_{0,k} = D_k$. Our misfit criterion then reads:

$$\mathcal{P}_n = \sum_{k=1}^{N_{\rm pixel}} W_k \, \left[R_{n-1,k} - I_0 + \alpha_n \, g_n(X'_k, Y'_k)\right]^2 . \quad (15)$$

Optimizing only on the new particle parameters rather than fitting all parameters for all particles yields a significant speed up in the algorithm. To achieve ultimate detection sensitivity, we however always perform a local fit with respect to all the parameters whenever no significant particle can be detected in the residuals. In practice, we have observed that this strategy is much faster and yields almost the same results as if I_0 and all the parameters of all the particles were refined at every step.

Second, since the model is linear with respect to I_0 and α_n we can simply derive their optimal values, say I_0^+ and α_n^+, by simple linear regression given the coordinates (x', y', z') and radius r' of the sought particle. This reduces the number of explicit parameters to adjust to $\{x'_n, y'_n, z'_n, r'_n\}$ and we define:

$$\begin{aligned} \mathcal{P}_n^+ &= \mathcal{P}_n|_{I_0=I_0^+, \alpha_n=\alpha_n^+} \\ &= \sum_{k=1}^{N_{\rm pixel}} W_k \, \left[R_{n-1,k} - I_0^+ + \alpha_n^+ \, g_n(X'_k, Y'_k)\right]^2 \quad (16) \end{aligned}$$

with:

$$\begin{aligned} I_0^+ &= \frac{1}{Q_n} \left(\sum\nolimits_k W_k \, G_{n,k}^2\right) \left(\sum\nolimits_k W_k \, R_{n-1,k}\right) \\ &\quad - \frac{1}{Q_n} \left(\sum\nolimits_k W_k \, G_{n,k}\right) \left(\sum\nolimits_k W_k \, R_{n-1,k} \, G_{n,k}\right) \quad (17) \\ \alpha_n^+ &= \frac{1}{Q_n} \left(\sum\nolimits_k W_k \, G_{n,k}\right) \left(\sum\nolimits_k W_k \, R_{n-1,k}\right) \\ &\quad - \frac{1}{Q_n} \left(\sum\nolimits_k W_k\right) \left(\sum\nolimits_k W_k \, R_{n-1,k} \, G_{n,k}\right) , \quad (18) \end{aligned}$$

where $G_{n,k} = g_n(X'_k, Y'_k)$ and:

$$Q_n = \left(\sum\nolimits_k W_k\right) \left(\sum\nolimits_k W_k \, G_{n,k}^2\right) - \left(\sum\nolimits_k W_k \, G_{n,k}\right)^2 . \quad (19)$$

The minimization of $\mathcal{P}_n^+$ with respect to x'_n, y'_n, z'_n and r'_n is then performed by a trust-region Newton algorithm[18]. Such an algorithm requires a local quadratic approximation of the penalty function $\mathcal{P}_n^+$ which is provided by the first and second order partial derivatives of the penalty with respect to the parameters. The computation of these partial derivatives and further approximation which can be made in our particular case are detailed in Appendix A.

C. Algorithm summary

The different stages of our iterative algorithm are summarized in Fig. 3. We expect that the coarse localization step followed by the local optimization step effectively solve the global optimization problem of finding the best size and location of a particle in the (residual) hologram image. A typical run of the algorithm on real data is shown by Fig. 6.

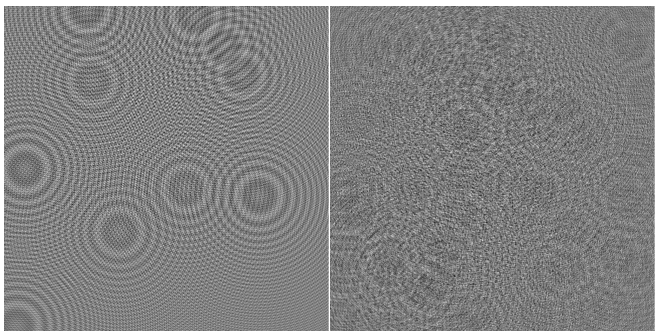

Fig. 4. Small particles simulations. Left: 10 particles; right: 100 particles.

When a hologram image is processed, the patterns due to particles other than the one of interest contribute as a kind of noise which can bias the localization of the particle of interest. It can even prevent its detection if its own signature is too faint. This can strongly limit the sensitivity of conventional algorithms. By repeating the detection and localization steps after removal of previously detected particles, we expect that our algorithm will be able to find particles with very faint signatures.

Since our algorithm was derived following an inverse problem approach, it does not require any explicit direct inversion of the observed hologram: all required comparisons are made in the data space. As a result, our algorithm has a number of advantages over other existing methods. For instance, our method is insensitive to the twin-image problem inherent in in-line holography. Moreover, our algorithm even does not suffer from bias for particles found close to the borders of the field of view.

4. Results

A. Simulated data

We first used simulated data to assess the actual performances of our algorithm under various conditions. To check the robustness with respect to the particle density, we considered two different concentrations: 10 and 100 particles per hologram. To evaluate the influence of the particle size on the precision of the measured depth and particle diameter, we used two different typical particle sizes: the so-called large ones and the so-called small ones. The first particle configuration consisted of realistic conditions close to those of the experimental test (see Sec. 4 B) with particles of radius between 35 µm and 50 µm at about 100 mm of the camera. In the second particle configuration, we simulated smaller particles with radii from 3.5 µm to 5 µm at a distance of about 250 mm from the camera such that the approximations made in Sec. 2 remain valid. All simulations were made for a 1024×1024 camera with a $6.70\,\mu\text{m} \times 6.70\,\mu\text{m}$ pixel and a

Table 1. Root mean squared errors for the estimated particle parameters in several simulation configurations.

configuration	Δx (µm rms)	Δy (µm rms)	Δz (µm rms)	Δr (µm rms)
10 large particles	0.27	0.26	0.74	0.06
100 large particles	0.30	0.30	2.37	0.12
10 small particles	0.28	0.28	0.26	0.15
100 small particles	0.28	0.29	0.85	0.51

large particles are for $35\,\mu\text{m} \leq r \leq 50\,\mu\text{m}$ and *small* particles are for $3.5\,\mu\text{m} \leq r \leq 5\,\mu\text{m}$.

laser of wavelength 632.8 nm. The volume of interest for the detection was a box of 8 mm × 8 mm × 30 mm. Examples of simulated images for the small particles case at two different concentrations are shown in Fig. 4.

Our inverse problem approach is based on a simplified model of the hologram image formation. To account for the effects of such simplifications on the detection and localization of the particles, we use a more accurate model to simulate the hologram images used in this test. More precisely, we use the image model given by Eq. 8 to simulate the holograms whereas the simplified model in Eq. 9 is assumed during the detection and localization steps of the algorithm. Hence the interference pattern between waves diffracted by different particles is accounted for in the simulated images whereas it is neglected by the algorithm. In order to properly simulate quantization by the detector, the simulated hologram images are converted into 8-bit integer values prior to their processing.

In the particle detection step (described section in 3 A), a reconstruction every millimeter in z was sufficient for a correct coarse detection. The parameters estimated by our algorithm on the simulated images under the various conditions were compared to their actual values. No significant bias was noticed and the corresponding root mean squared (RMS) errors are listed in Tab. 1. These results mainly demonstrate the excellent precision achieved by our algorithm under all the considered conditions. Our method seems to be efficient with densities up to 100 particles per hologram.

Sub-pixel precision is reached for the transversal position with $\Delta x \simeq \Delta y \simeq 0.3\,\mu\text{m}$ or $1/20$ pixel. This transversal precision does not significantly depend on the size and density of the particles.

Increasing the number of particles strengthens the interference between diffracted waves which are neglected in the assumed model. This also increases the occurences of particles almost aligned along the depth direction. These two effects worsen the precision of the estimated depth and particle radius.

The high spatial frequency diffraction rings help to precisely locate the depth of the particles. Since these rings are attenuated as the size of the particles grow, the longitudinal errors are worse for bigger particles. On the other hand, this attenuation favors the determination of the particle radius.

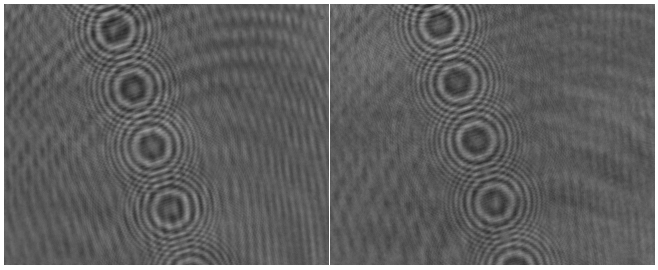

Fig. 5. Pair of experimental holograms separated by a delay of 100 µs.

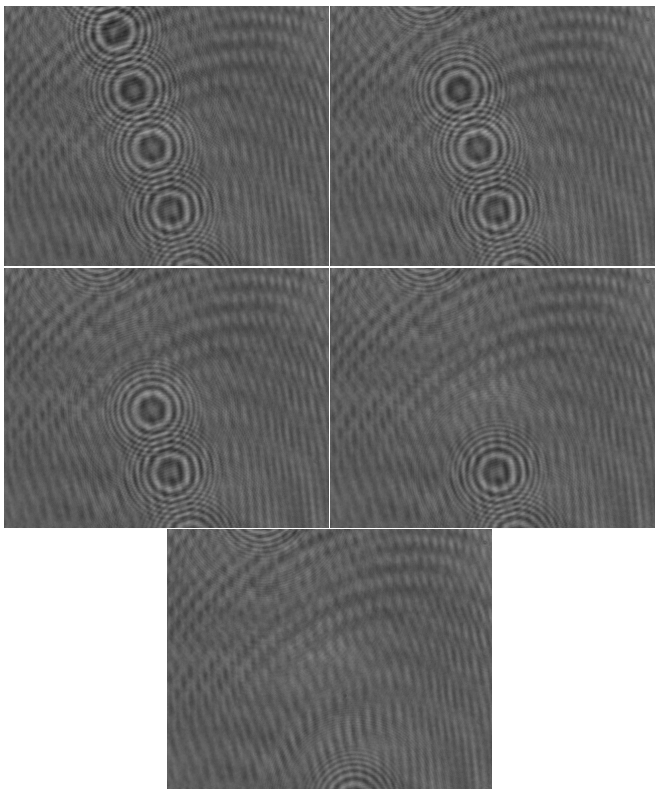

Fig. 6. Iterative particle removal in real hologram image. From top left to bottom: initial hologram image $R_0 = D$ and residual images R_1, R_2, R_3 and R_4 after detection and removal of 0, 1, 2, 3 and 4 particles respectively.

In Sec. 3 C we argued that the position errors should not be biased for particles near the edges of the field of view. In our simulations, we have measured no differences in the precision of the tri-dimensional particle positions wherever their actual locations were.

B. Experimental data

We carried out an experimental test of our algorithm using real data from an in-line holography setup. The experimental layout is shown by Fig. 1 and the components

are as follows:

The laser is a double cavity YAG (ULTRA-PIV 30, Quantel) with a 0.532 µm wavelength. It emits pulses of 7 ns short enough to freeze the droplets motion. The laser is synchronized with the camera to trigger the acquisition of pairs of hologram images separated by a delay of 100 µs. This is intended to allow for the measurement of the instantaneous velocity of the particles.

The injector is a piezoelectric device which generates monodisperse droplets. The droplet diameter is tunable from 50 µm to 100 µm. The injector can work in droplet-on-demand mode, generating droplets at constant time intervals (1000 Hz in the case of the considered data set).

The camera is a 12-bit CCD (PCO Sensicam) with 1280×1024 pixels of size $6.7\,\mu\text{m} \times 6.7\,\mu\text{m}$. The camera is at about 25 cm of the injector in order not to disturb the flow experiment. This leads to a small but realistic numerical aperture of $\Omega = 0.014$.

The experimental test data consists of a set of 100 pairs of holograms with four or five droplets on each image. An example of such a pair is shown in Fig. 5. The 3-D positions and diameters of droplets were extracted from this data set by our algorithm. Figure 6 shows the residual images during the processing of one of the experimental hologram.

The measured particles positions are shown in Fig. 7 under various projections. Clearly the average trajectory of the particles is a straight line as can be expected from the experimental conditions. In Fig. 7, ζ denotes the direction of this line. It is important to notice that the trajectory of the droplets is recovered with the same precision in the transversal (x, y) plane than in the longitudinal (ζ, z) plane. These observed deviations from the ideal straight trajectory (66 µm in (x, y) plane and 58 µm in (ζ, z) plane) are however mostly due to real physical effects. Indeed the oscillations and the beam divergence which can be seen in Fig. 7 are due to vibrations of the injector. Hence the effective precision of the measured positions is smaller than the variations due to these physical effects.

The droplet sizes estimated by our algorithm have a bell-shaped distribution (see Fig. 8) with a mean diameter of 94.1 µm and a standard deviation of 0.3 µm in agreement with the settings of the droplet injector.

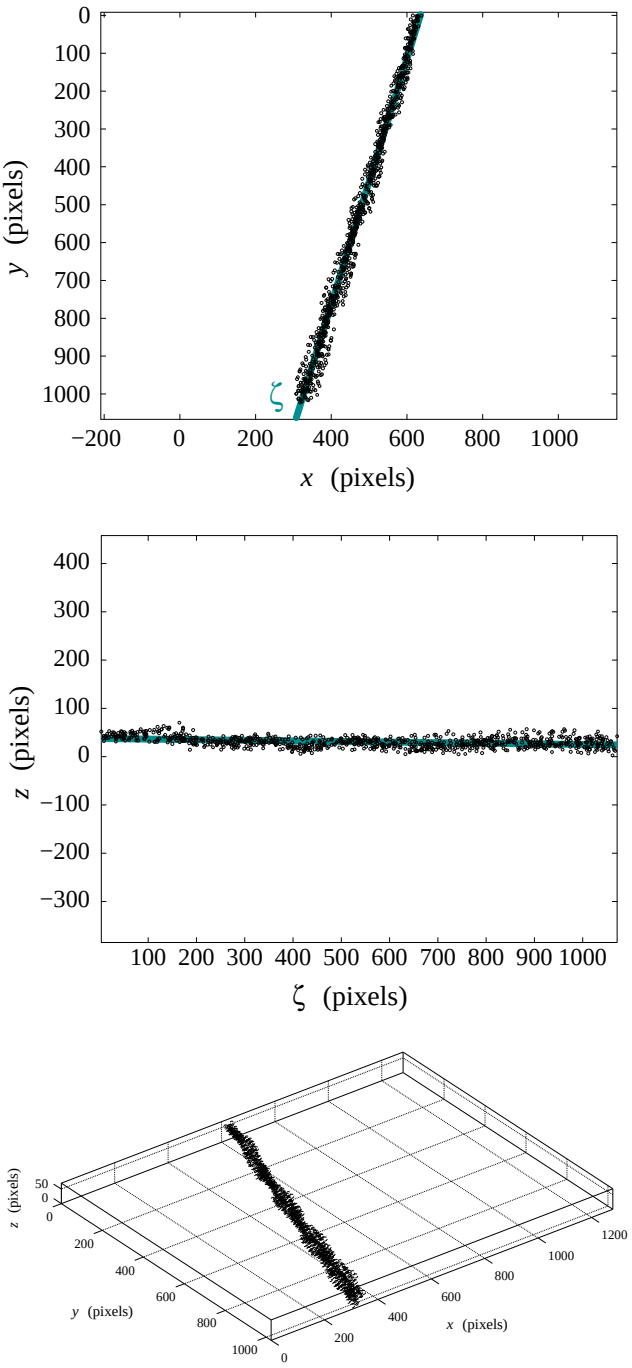

Fig. 7. Droplets jet reconstruction. From top to bottom: (x, y) view, (ζ, z) view and 3-D representation of segmented droplets. The best fit line is represented as a gray thick line.

5. Discussion

In this paper we describe a new algorithm for the detection and localization of particles in digital holography. The most important difference with other existing techniques is that our processing is based on an inverse problem approach and does not require any direct inversion. In this framework, we introduce a simplified model of the hologram images which depends on the sizes and positions of the diffracting particles. We then solve the problem by seeking for the set of particle parameters for which the difference between the model and the data is statistically minimal. Such a criterion turns out to have multiple local minima and thus global optimization is

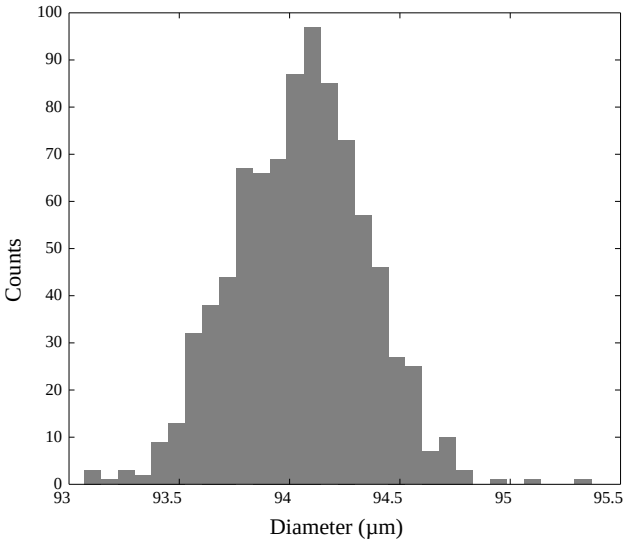

Fig. 8. Measured diameters histogram

required to properly solve the problem. Our algorithm effectively achieves the global minimum by performing an approximative detection of the particles in the whole parameter space followed by a local refinement of the parameters. By repeating these steps on the residual images, obtained by subtracting the model to the data, our algorithm is able to detect several particles even the ones which have a faint signature compared to the diffraction pattern due to the other particles.

We have tested our algorithm on simulated and real data. Our results show that the precision along the depth direction is largely improved and is much better than the optical resolution in such conditions ($\delta z \geq \lambda/\Omega^2 = 2.6\,\mathrm{mm}$). From our simulations, we get a depth precision as good as $\Delta z = 0.3\,\mu\mathrm{m}$, comparable to the transversal precision, for low particle density and small particle sizes. As expected, the depth precision is degraded as the density and/or the size of the particles increase. On the contrary, we found that the transversal precision achieved by our algorithm, $\Delta x = \Delta y = 0.3\,\mu\mathrm{m}$ in the conditions of our simulations, does not significantly depend on the particle density, nor on the particle sizes.

Being based on an inverse problem approach, an important property of our algorithm among the other existing methods is that it has no particular bias for particles near the edges of the field of view (*i.e.* the ones with the most truncated signatures). Indeed we have found no significant degradation of the precision in the measured positions for the most distant particles from the center of the field of view. As a result, the effective field of view can be extended to account for the whole area of the detector and not just its central part. Similarly, our algorithm can account for bad data or non-rectangular holograms by setting to zero the weights of bad pixels or pixels outside the area covered by the detector.

Not only the simplifications made in the model assumed by the proposed method are not an issue but, when dealing with real data, it appears that our algorithm is also robust with respect to non-homogeneous illumination and to spurious patterns as the CCD fringes which can be seen in the last residual image of Fig. 6. In principle, it is possible to use the same algorithm with a different model to account for more complex or more realistic experimental conditions. For instance, we can use a diffraction model for fibers or elongated particles with 7 parameters per particle: 3-D position, width, length, and orientation angles. This may however have a prohibitive impact on the memory and on the processing time required by the method.

The actual sensitivity of the detection is largely improved by iteratively working on the residual images. This allows us to correctly detect and locate particles with densities as high as 100 particles per hologram. The maximum density achievable by our algorithm has yet to be estimated, *e.g.* from further simulations. To allow for this study, we however need to improve the speed of our algorithm. The processing time scales as the number of particles per hologram image. For the present experiments, with a Pentium IV CPU 3.60 GHz with 2 GBytes of RAM our algorithm took 7 minutes per particle: 4 minutes for the detection and 3 minutes for particle parameters refinement. We plan to greatly reduce this time by performing multiple detections per pass of our iterative algorithm. We also expect a speedup by a factor of roughly two thanks to trivial computational optimizations such as using faster numerical routines to compute the Bessel functions. The routinely processing of large number of holograms would also benefit from these improvements.

Appendix A: Partial derivatives

In this appendix we detail the computation of the partial derivatives of the penalty $\mathcal{P}_n^+$ with respect to the sought parameters. Such derivatives are required to approximately describe the behaviour of the penalty function in the parameter space so that the trust region Newton algorithm[18] can derive a change of parameter to reduce the penalty.

By applying the chaining rule, the partial derivative of the penalty $\mathcal{P}_n^+$ with respect to a parameter θ (where θ can be x'_n, y'_n, z'_n or r'_n) writes:

$$\frac{\partial \mathcal{P}_n^+}{\partial \theta} = \left.\frac{\partial \mathcal{P}_n}{\partial \theta}\right|_{\substack{I_0=I_0^+ \\ \alpha_n=\alpha_n^+}} + \frac{\partial \alpha_n^+}{\partial \theta}\left.\frac{\partial \mathcal{P}_n}{\partial \alpha_n}\right|_{\substack{I_0=I_0^+ \\ \alpha_n=\alpha_n^+}} + \frac{\partial I_0^+}{\partial \theta}\left.\frac{\partial \mathcal{P}_n}{\partial I_0}\right|_{\substack{I_0=I_0^+ \\ \alpha_n=\alpha_n^+}} .$$

However, since:

$$\{\alpha_n^+, I_0^+\} = \underset{\alpha_n, I_0}{\arg\min}\, \mathcal{P}_n \,,$$

the partial derivatives of $\mathcal{P}_n$ with respect to α_n and I_0 exactly cancel at α_n^+ and I_0^+. The partial derivative of

$\mathcal{P}_n^+$ therefore simplifies to:

$$\frac{\partial \mathcal{P}_n^+}{\partial \theta} = \left.\frac{\partial \mathcal{P}_n}{\partial \theta}\right|_{\substack{I_0=I_0^+ \\ \alpha_n=\alpha_n^+}} = 2\,\alpha_n^+ \sum_{k=1}^{N_{\text{pixel}}} W_k \left[R_{n-1,k} - I_0^+ + \alpha_n^+\, g_{n,k}\right] \frac{\partial g_{n,k}}{\partial \theta} \quad \text{(A1)}$$

where $g_{n,k} = g_n(X'_k, Y'_k)$ of which the partial derivatives are:

$$\frac{\partial g_{n,k}}{\partial x'_n} = \frac{\left(x'_n - X'_k\right) r'_n}{2\,{\rho'_{n,k}}^3} \left[\phi_{n,k}\ \mathrm{J}_0(\phi_{n,k})\ \sin\theta_{n,k} - 2\ \mathrm{J}_1(\phi_{n,k})\ \left(\sin\theta_{n,k} - \theta_{n,k}\ \cos\theta_{n,k}\right)\right] \quad \text{(A2)}$$

$$\frac{\partial g_{n,k}}{\partial y'_n} = \frac{\left(y'_n - Y'_k\right) r'_n}{2\,{\rho'_{n,k}}^3} \left[\phi_{n,k}\ \mathrm{J}_0(\phi_{n,k})\ \sin\theta_{n,k} - 2\ \mathrm{J}_1(\phi_{n,k})\ \left(\sin\theta_{n,k} - \theta_{n,k}\ \cos\theta_{n,k}\right)\right] \quad \text{(A3)}$$

$$\frac{\partial g_{n,k}}{\partial z'_n} = \frac{r'_n}{2\,\rho'_{n,k}\,z'_n} \left[\mathrm{J}_1(\phi_{n,k})\ \left(\sin\theta_{n,k} - \theta_{n,k}\ \cos\theta_{n,k}\right) - \phi_{n,k}\ \mathrm{J}_0(\phi_{n,k})\ \sin\theta_{n,k}\right] \quad \text{(A4)}$$

$$\frac{\partial g_{n,k}}{\partial r'_n} = \frac{\pi\, r'_n}{z'_n}\ \mathrm{J}_0(\phi_{n,k})\ \sin\theta_{n,k} \quad \text{(A5)}$$

with

$$\theta_{n,k} = \frac{\pi\,{\rho'_{n,k}}^2}{z'_n} \quad \text{(A6)}$$

$$\phi_{n,k} = \frac{2\,\pi\, r'_n\, \rho'_{n,k}}{z'_n} \quad \text{(A7)}$$

$$\rho'_{n,k} = \sqrt{\left(x'_n - X'_k\right)^2 + \left(y'_n - Y'_k\right)^2}\,. \quad \text{(A8)}$$

Exact computation of the second order partial derivatives would require the partial derivatives of α_n^+ and I_0^+ and the first and second order partial derivatives of $g_{n,k}$. A nice property of descent minimization methods such as the trust region Newton algorithm is that they only need an approximation of the Hessian (matrix of second order partial derivatives). We make use of this feature to approximate the second order partial derivatives with respect to parameters θ_1 and θ_2 by:

$$\frac{\partial^2 \mathcal{P}_n^+}{\partial\theta_1\,\partial\theta_2} \simeq 2\,{\alpha_n^+}^2 \sum_{k=1}^{N_{\text{pixel}}} W_k \frac{\partial g_{n,k}}{\partial\theta_1} \frac{\partial g_{n,k}}{\partial\theta_2} \quad \text{(A9)}$$

which is somewhat reminiscent of Levenberg-Marquardt approximation in non-linear least squares. Thanks to our approximation, only the partial derivatives of $g_{n,k}$ with respect to the sought parameters x'_n, y'_n, z'_n and r'_n are required.

References

1. B. J. Thompson, "A new method of measuring particle size by diffraction techniques," Japanese Journal of Applied Physics **4**, 302–307 (1965).
2. C. S. Vikram, "Holographic Particle Diagnostics," in *SPIE Milestone*, vol. MS21 (1990).
3. K. D. Hinsch, "Holographic Particle Image Velocimetry," Measurement Science and Technology **13**, R61–R72 (2002).
4. T. M. Kreis, M. Adams, and W. Jüptner, "Methods of Digital Holography: A Comparison," SPIE (Munich, Germany, 1997).
5. M. Liebling, T. Blu, and M. Unser, "Fresnelets: New Multiresolution Wavelet Bases for Digital Holography," IEEE Transactions on image processing **12**, 29–43 (2003).
6. C. Fournier, C. Ducottet, and T. Fournel, "Digital in-line holography: influence of the reconstruction function on the axial profile of a reconstructed particle image," Measurement Science & Technology **15**, 686–693 (2004).
7. W. Yang *et al.* "Depth-of-Focus Reduction for Digital In-Line Holography of Particle Fields," Optics Letters **30**, 1303–1305 (2005).
8. L. Denis, C. Fournier, T. Fournel, and C. Ducottet, "Twin-image noise reduction by phase retrieval in in-line digital holography," in *Wavelets XI* (San Diego, CA, USA, 2005).
9. S. Murata and N. Yasuda, "Development of Full-volume Digital Holography for Particle Measurement," in *Optical Methods and Data Processing in Heat and Fluid Flow*, C. Greated, J. Buick, and J. Cosgrove, eds., pp. 698–77 (Professional Engineering Publishing, 2002).
10. M. Malek, D. Allano, S. Coëtmellec, and D. Lebrun, "Digital in-line holography: influence of the shadow density on particle field extraction," Optics Express **12**, 2270–2280 (2004).
11. G. Pan and H. Meng, "Digital holography of particle fields: reconstruction by use of complex amplitude," Applied Optics **42**, 827–833 (2003).
12. S. Murata and N. Takeuchi, "A neural network approach to the detection of the depth of tracer particles from in-line hologram patterns," in *IMechE* **53**, 377–382(1996).
13. L. Denis, C. Fournier, T. Fournel, C. Ducottet, and D. Jeulin, "Direct extraction of mean particle size from a digital hologram," Applied Optics **45**, 944–952 (2006).
14. C. S. Vikram, *Particle field holography* (Cambridge University Press, 1992).
15. S. Sotthivirat and J. A. Fessler, "Penalized-likelihood image reconstruction for digital holography," J. Opt. Soc. Am. A **21**(5), (2004).
16. J. W. Goodman, *Introduction to Fourier Optics* (Mc Graw-Hill, 1996).
17. G. A. Tayler and B. J. Thompson, "Fraunhofer holography applied to particle size analysis: a reassessment," Opt. Acta. **23**, 261–304 (1976).
18. J. J. Moré and D. C. Sorensen, "Computing A Trust Region Step," SIAM J. Sci. Stat. Comp. **4**(3), 553–572 (1983).